AIAA Guidance, Navigation and Control Conference, Toronto, Canada

Wind Field Estimation for Small Unmanned Aerial Vehicles

Jack W. Langelaan*
The Pennsylvania State University, University Park, PA 16802, USA
Nicholas Alley†
Area-I Inc., Canton, GA 30115 USA
James Neidhoefer‡
Aerotonomy, Inc., Lithia Springs, GA 30122 USA

This paper describes a method for estimating wind field (wind velocity, rate of change of wind velocity and wind gradient) for small and mini unmanned aerial vehicles. The approach utilizes sensors which are already part of a standard autopilot sensor suite (GPS, inertial measurement unit, airspeed, magnetometer). The primary motivation is enabling energy harvesting; a secondary motivation is development of a low-cost atmospheric measurement and sampling system. The paper presents an error analysis and discusses the primary contributions to error in the estimated wind field. Results of Monte Carlo simulations compare predicted errors in wind estimates with actual errors and show the effect of using estimated winds for energy harvesting from gusts.

I. Introduction

Interest in the problem of autonomous atmospheric energy harvesting (i.e. autonomous soaring) has been growing over the past few years. Observations of bird flight published by Lord Rayleigh in 1883 and 1889[1,2] provided the early indications of energy harvesting using appropriate flight techniques. More recent work by Pennycuick[3] and Sachs[4] quantified the conditions under which birds such as albatrosses are able to harvest energy.

Knowledge of wind field is generally implicitly assumed in autonomous energy harvesting research. Dynamic soaring typically assumes full *a priori* knowledge of the wind field and casts energy harvesting as a trajectory optimization problem,[5,6] and even gust soaring assumes knowledge of current wind conditions.[7,8]

This paper is concerned with estimating wind conditions to enable gust soaring. Since the motivation is small, low cost UAVs (here small is assumed to mean hand-launchable vehicles ranging from 1 kg mass/1m span to 10 kg mass/4m span), minimizing sensing requirements is a priority. For example, while accurate measurements of wind field (including spatial gradients) can be obtained using arrays of multi-hole pitot probes,[9] the intent here is to obtain estimates of wind field using only sensing that is already available on the aircraft. This sensing suite (included in typical autopilot modules) includes Global Positioning System (GPS), inertial measurement unit (IMU), magnetometer, static pressure and dynamic pressure. Here we further assume that the autopilot module computes an estimate of aircraft state (position, orientation and velocity with respect to the airmass). This estimate of state is not assumed to be perfect: in addition to estimation of the wind field, this paper discusses the effect of noise and errors in the state estimate on the computed wind field.

Dynamic soaring and efficient gust soaring can under certain conditions make significant use of gradients and rates of change of the wind field. Hence the wind estimation system must be able to obtain estimates of gradients and rates of change of wind velocity as well as the components of wind velocity.

*Assistant Professor, Department of Aerospace Engineering, Senior Member AIAA.
†Member AIAA.
‡Associate Fellow AIAA.

A significant amount of research has been conducted for wind estimation. Pachter et al. use GPS inertial and air data measurements to estimate horizontal components of wind speed and vehicle heading angle, but do not address wind gradients or acceleration.[10] Rodriguez et al. use GPS, air data and optical flow to compute wind speed for planar flight.[11] Myschik discusses an integrated wind estimation/navigation system for use on general aviation aircraft.[12,13] de Divitiis describes a variational technique for wind estimation for a small ducted fan vehicle.[14]

II. Wind Estimation

A. Wind field

Wind is assumed to be a spatially and temporally varying vector field:

$$\mathbf{w}(x,y,z,t) = \begin{bmatrix} w_{ix}(x,y,z,t) \\ w_{iy}(x,y,z,t) \\ w_{iz}(x,y,z,t) \end{bmatrix} \tag{1}$$

where the subscript i denotes components expressed in the inertial frame. A vehicle flying through this field is influenced by the components of the wind field, local temporal variations of the wind field and by gradients of the wind field. The rate of change of wind velocity as seen by the vehicle is a function of the rate of change of wind speed at a point, the field gradient and the vehicle velocity:

$$\frac{d}{dt}\mathbf{w}(x,y,z) = \begin{bmatrix} \dot{w}_{ix} \\ \dot{w}_{iy} \\ \dot{w}_{iz} \end{bmatrix} = \begin{bmatrix} \dot{w}^l_{ix} \\ \dot{w}^l_{iy} \\ \dot{w}^l_{iz} \end{bmatrix} + \nabla\mathbf{w} \begin{bmatrix} \dot{x} \\ \dot{y} \\ \dot{z} \end{bmatrix} \tag{2}$$

where $\dot{x}$, $\dot{y}$, $\dot{z}$ are the components of the velocity of the vehicle with respect to the inertial frame and $\nabla\mathbf{w}$ is the spatial gradient of the wind field. The superscript l denotes the time rate of change of wind velocity at the point (x,y,z). For a frozen wind field this is zero, however the approximation of a frozen wind field is only applicable when vehicle velocity is large compared with the "point" rates of change of wind velocity.

Unless arrays of air data probes are used, separating the effect of gradients from the point rates of change is extremely difficult without making several approximations and simplifications. MIL-F-8785C suggests treating wind gradients as equivalent to aircraft angular velocities, with

$$p_w = -\frac{\delta w_{bz}}{\delta y} \tag{3}$$

$$q_w = \frac{\delta w_{bz}}{\delta x} \tag{4}$$

$$r_w = \frac{\delta w_{by}}{\delta x} \tag{5}$$

where the subscript b denotes components of wind expressed in the body frame.[15]

This definition assumes that the effects of some components of gradient are negligible because of typical aircraft configuration: for example, wing span is significantly larger than tail height, so vertical gradient of the lateral airmass velocity has negligible effect on roll rate.

Depending on the ultimate application of the wind field estimates it may be unnecessary to separate the effect of point changes in wind speed from the effect of gradients. This paper will focus on the problem of estimating the velocity vector and the net rate of change of wind velocity.

B. Vehicle Dynamics and Kinematics

Equations of motion of a flight vehicle in turbulent conditions are briefly derived. Consider an aircraft located at $\mathbf{r}$ in an inertial frame I, where $\hat{x}^i$, $\hat{y}^i$ and $\hat{z}^i$ define unit vectors (see Figure 1).

Using a standard body-fixed coordinate frame with airmass-relative velocity $\mathbf{v}_a$ having components u, v, w in the body $\hat{x}_b$, $\hat{y}_b$, $\hat{z}_b$ directions, respectively, the velocity of the aircraft in the inertial frame is

$$\dot{\mathbf{r}} = \mathbf{v}_a + \mathbf{w} \tag{6}$$

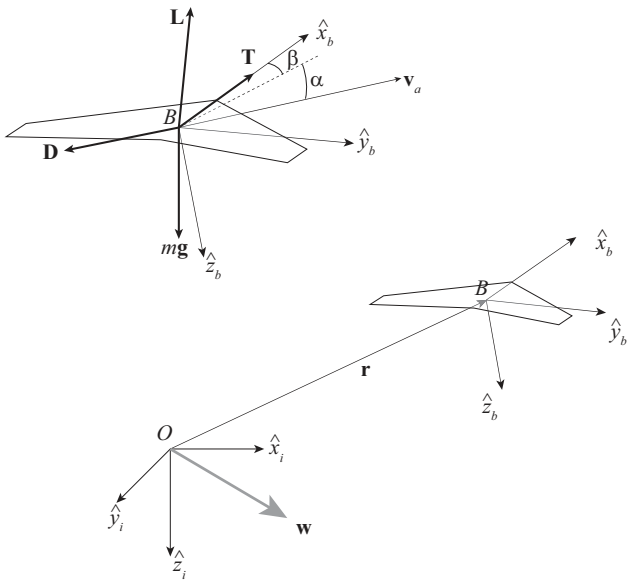

Figure 1. Reference frames. The upper left portion shows forces acting on the vehicle.

Hence

$$\ddot{\mathbf{r}} = \frac{\mathrm{d}}{\mathrm{d}t}\mathbf{v}_a + \frac{\mathrm{d}}{\mathrm{d}t}\mathbf{w} \tag{7}$$

where

$$\frac{\mathrm{d}}{\mathrm{d}t}\mathbf{v}_a = \begin{bmatrix} \dot{u} \\ \dot{v} \\ \dot{w} \end{bmatrix} + \boldsymbol{\omega} \times \mathbf{v}_a \tag{8}$$

Note that coordinate frames in Equation 6 have not yet been specified: for convenience the inertial frame O is used for $\mathbf{w}$ while the body-fixed frame is used for $\mathbf{v}_a$.

Substituting $\boldsymbol{\omega} = [p\ q\ r]^T$ (the angular velocity expressed in the body frame),

$$\mathbf{X} + \mathbf{Y} + \mathbf{Z} + m\mathbf{g} = m\left[(\dot{u} + qw - rv)\hat{x}_b + (\dot{v} + ru - pw)\hat{y}_b + (\dot{w} + pv - qu)\hat{z}_b + \frac{\mathrm{d}}{\mathrm{d}t}\mathbf{w}\right] \tag{9}$$

where $\mathbf{X}$, $\mathbf{Y}$, and $\mathbf{Z}$, are aerodynamic forces in the body x, y, z directions, respectively (these are functions of thrust $\mathbf{T}$, drag $\mathbf{D}$ and lift $\mathbf{L}$) and $m\mathbf{g}$ is the force due to gravity.

The vector of wind accelerations $\frac{\mathrm{d}}{\mathrm{d}t}\mathbf{w}$ is expressed in the inertial frame. Using a direction cosine matrix $\mathbf{T}$ which transforms a vector expressed in the inertial frame to a vector expressed in the body frame,

$$\mathbf{T} = \begin{bmatrix} \cos\theta\cos\psi & \cos\theta\sin\psi & -\sin\theta \\ \sin\phi\sin\theta\cos\psi - \cos\phi\sin\psi & \sin\phi\sin\theta\sin\psi + \cos\phi\cos\psi & \sin\phi\cos\theta \\ \cos\phi\sin\theta\cos\psi + \sin\phi\sin\psi & \cos\phi\sin\theta\sin\psi - \sin\phi\cos\psi & \cos\phi\cos\theta \end{bmatrix} \tag{10}$$

the body axis accelerations with respect to the surrounding air are

$$\dot{u} = \frac{X}{m} - g\sin\theta - qw + rv - \dot{w}_{ix}\cos\theta\cos\psi - \dot{w}_{iy}\cos\theta\sin\psi + \dot{w}_{iz}\sin\theta \tag{11}$$

$$\dot{v} = \frac{Y}{m} + g\sin\phi\cos\theta + pw - ru - \dot{w}_{ix}(\sin\phi\sin\theta\cos\psi - \cos\phi\sin\psi) - \dot{w}_{iy}(\sin\phi\sin\theta\sin\psi + \cos\phi\cos\psi) - \dot{w}_{iz}\sin\phi\cos\theta \tag{12}$$

$$\dot{w} = \frac{Z}{m} + g\cos\phi\cos\theta + qu - pv - \dot{w}_{ix}(\cos\phi\sin\theta\cos\psi + \sin\phi\sin\psi) - \dot{w}_{iy}(\cos\phi\sin\theta\sin\psi - \sin\phi\cos\psi) - \dot{w}_{iz}\cos\phi\cos\theta \tag{13}$$

Here $\dot{w}_{i(\cdot)}$ denotes the rate of change of a component of the wind velocity expressed in the inertial frame.

Given the vehicle dynamics in Equations 11–13, expressions for aerodynamic forces are required. Here linearized expressions for forces and moments are used, so that[16]

$$X = X_0 + X_u\Delta u + X_w\Delta w + X_c \tag{14}$$
$$Y = Y_0 + Y_v v + Y_p(p - p_w) + Y_r(r - r_w) + Y_c \tag{15}$$
$$Z = Z_0 + Z_u\Delta u + Z_w\Delta w + Z_{\dot{w}}\dot{w} + Z_q(q - q_w) + Z_c \tag{16}$$

Stability and control derivatives are vehicle dependent.

Finally, aircraft kinematics with respect to the Earth are

$$\begin{bmatrix} \dot{x} \\ \dot{y} \\ \dot{z} \end{bmatrix} = \mathbf{T}^{-1} \begin{bmatrix} u \\ v \\ w \end{bmatrix} + \begin{bmatrix} w_{ix} \\ w_{iy} \\ w_{iz} \end{bmatrix} \tag{17}$$

where $\dot{x}$, $\dot{y}$, $\dot{z}$ are the components of aircraft velocity with respect to the Earth in the Earth-fixed (i.e. inertial) reference frame, $\mathbf{T}$ is the direction cosine matrix (Equation 10), u, v, w are components of the aircraft velocity with respect to the airmass expressed in the body frame and w_{ix}, w_{iy}, w_{iz} are the components of the wind speed with respect to the Earth, expressed in the inertial reference frame.

C. Computing Wind from Vehicle Response

Rather than use a Kalman Filter framework to estimate wind field in conjunction with aircraft states, one can compare measurements of aircraft motion with respect to the Earth with predictions of aircraft motion obtained from the dynamic model. The aircraft equations of motion can be separated into two parts: motion induced by the state and control inputs and motion induced by the wind field. Beginning with the equations for vehicle dynamics (Equations 11–13), and kinematics (Equation 17),

$$\begin{bmatrix} \dot{x} \\ \dot{y} \\ \dot{z} \end{bmatrix} = \mathbf{T}^{-1} \begin{bmatrix} u \\ v \\ w \end{bmatrix} + \begin{bmatrix} w_{ix} \\ w_{iy} \\ w_{iz} \end{bmatrix} \tag{18}$$

$$\begin{bmatrix} \dot{u} \\ \dot{v} \\ \dot{w} \end{bmatrix} = \begin{bmatrix} \frac{X}{m} - g\sin\theta - qw + rv \\ \frac{Y}{m} + g\sin\phi\cos\theta + pw - ru \\ \frac{Z}{m} + g\cos\phi\cos\theta + qu - pv \end{bmatrix} - \mathbf{T} \begin{bmatrix} \dot{w}_{ix} \\ \dot{w}_{iy} \\ \dot{w}_{iz} \end{bmatrix} \tag{19}$$

Writing this compactly in discrete form using a Forward Euler integration,

$$\mathbf{x}_k = \mathbf{x}_{k-1} + \Delta t f_u(\mathbf{x}_{k-1}, \mathbf{u}_{k-1}) + \Delta t \begin{bmatrix} \mathbf{I} & 0 \\ 0 & -\mathbf{T} \end{bmatrix} \begin{bmatrix} \mathbf{w}_{k-1} \\ \dot{\mathbf{w}}_{k-1} \end{bmatrix} \tag{20}$$

where $\mathbf{x} = [x\ y\ z\ u\ v\ w]^T$ and f_u is the aircraft kinematic/dynamic model (i.e. the first terms on the right hand side of Equations 18 and 19). Rearranging gives the wind field:

$$\begin{bmatrix} \mathbf{w}_{k-1} \\ \dot{\mathbf{w}}_{k-1} \end{bmatrix} = \frac{1}{\Delta t} \begin{bmatrix} \mathbf{I} & 0 \\ 0 & -\mathbf{T}^{-1} \end{bmatrix} [\mathbf{x}_k - \mathbf{x}_{k-1} - \Delta t f_u(\mathbf{x}_{k-1}, \mathbf{u}_{k-1})] \tag{21}$$

This will compute the average value of wind velocity and wind acceleration over the time interval from $k-1$ to k. The quantity $\Delta t f_u(\mathbf{x}_{k-1}, \mathbf{u}_{k-1})$ is the prediction of the change in aircraft state over the time interval from $k-1$ to k while ignoring the effects of wind.

In principle this approach is straightforward, since the state $\mathbf{x}$ can be measured directly (using GPS for position and air data sensors for airspeedss). In practice, however, it is not likely to give good results. Its main fault is reliance on numerical differentiation of GPS position measurements: even with WAAS augmentation GPS uncertainty is of order 3m. While carrier phase differential GPS improves position accuracy to order centimeters, this is still significantly noisier than GPS velocity estimates. Further, this approach relies on an accurate dynamic model (this can be problematic for a small, low-cost UAV) and accurate state estimates for computing a prediction of vehicle state.

D. Direct Computation of Wind Field

A better approach is to use GPS velocity (which is not obtained by numerically differentiating position measurements, but by using the rates of change of pseudoranges) and measurements of vehicle acceleration. Combined with vehicle state information this can be used to directly compute the wind field.

1. *Wind Velocity*

GPS provides a direct measurement of velocity with respect to the Earth accurate to approximately 0.1 m/s (unaided: incorporating carrier phase differential GPS allows velocity measurements accurate to order mm/s).[17] Thus local airmass velocity components can be obtained directly from vehicle kinematics and the GPS velocity:

$$\begin{bmatrix} w_{ix} \\ w_{iy} \\ w_{iz} \end{bmatrix} = \begin{bmatrix} \dot{x} \\ \dot{y} \\ \dot{z} \end{bmatrix}_{GPS} - \mathbf{T}^{-1} \begin{bmatrix} u \\ v \\ w \end{bmatrix} \tag{22}$$

This assumes that the autopilot module provides estimates of the components of airspeed and Euler angles (ϕ, θ, ψ). The effect of noise in GPS velocity measurements and in estimates of orientation and airspeed on the computed wind will be discussed later.

2. *Rate of change of wind velocity (wind acceleration)*

The inertial measurement unit (IMU) provides measurements of body-axis acceleration with respect to the inertial frame and the gravity vector projected into the body frame.

$$\mathbf{z}_{imu} = \frac{\mathrm{d}}{\mathrm{d}t}\mathbf{v}_i - \mathbf{T}\mathbf{g} + \mathbf{b}_{imu} + \mathbf{n}_{imu} \tag{23}$$

where $\mathbf{v}_i$ is the velocity of the IMU with respect to the Earth expressed in the body frame, $\mathbf{b}_{imu}$ is the IMU bias (assumed known) and $\mathbf{n}_{imu}$ is zero-mean Gaussian random noise. Assuming the IMU is located at the aircraft center of gravity, substituting vehicle dynamics gives

$$\mathbf{z}_{imu} = \begin{bmatrix} a_{x,b} \\ a_{y,b} \\ a_{z,b} \end{bmatrix} = \begin{bmatrix} \dot{u} + \dot{w}_{x,b} + qw - rv + g\sin\theta \\ \dot{v} + \dot{w}_{y,b} + ru - pw - g\cos\theta\sin\phi \\ \dot{w} + \dot{w}_{z,b} + pv - qu - g\cos\theta\cos\phi \end{bmatrix} + \mathbf{b}_{imu} + \mathbf{n}_{imu} \tag{24}$$

Here the wind acceleration is expressed in the body frame. Rearranging gives

$$\begin{bmatrix} \dot{w}_{x,b} \\ \dot{w}_{y,b} \\ \dot{w}_{z,b} \end{bmatrix} = \begin{bmatrix} a_{x,b} - qw + rv - g\sin\theta - b_{imu,x} - \dot{u} \\ a_{y,b} - ru + pw + g\cos\theta\sin\phi - b_{imu,y} - \dot{v} \\ a_{z,b} - pv + qu + g\cos\theta\cos\phi - b_{imu,z} - \dot{w} \end{bmatrix} + \mathbf{n}_{imu} \tag{25}$$

where $b_{imu,(\cdot)}$ denotes the components of the accelerometer bias.

There is no direct measurement of the rate of change of airspeed ($\dot{u}$, $\dot{v}$, $\dot{w}$) and no means of predicting the rate of change of airspeed. Hence it must be computed by numerically differentiating measurements. This will be noisy, leading to potentially significant uncertainty in the computed values of rate of change of wind speed. It will also introduce a delay in the computation of wind acceleration. Here a second order numerical differentiation is used, so that

$$\begin{bmatrix} \dot{u} \\ \dot{v} \\ \dot{w} \end{bmatrix}_{k-1} = \frac{1}{2\Delta t} \begin{bmatrix} u_k - u_{k-2} \\ v_k - v_{k-2} \\ w_k - w_{k-2} \end{bmatrix} \tag{26}$$

where k denotes the current time step. Substituting into Equation 25 allows computation of the wind acceleration at the previous time step:

$$\begin{bmatrix} \dot{w}_{x,b} \\ \dot{w}_{y,b} \\ \dot{w}_{z,b} \end{bmatrix}_{k-1} = \begin{bmatrix} a_{x,b} - b_{imu,x} - g\sin\theta \\ a_{y,b} - b_{imu,y} + g\cos\theta\sin\phi \\ a_{z,b} - b_{imu,z} + g\cos\theta\cos\phi \end{bmatrix}_{k-1} - \begin{bmatrix} qw - rv \\ pw - ru \\ qu - pv \end{bmatrix}_{k-1} - \frac{1}{2\Delta t} \begin{bmatrix} u_k - u_{k-2} \\ v_k - v_{k-2} \\ w_k - w_{k-2} \end{bmatrix} \tag{27}$$

The difference between this approach and that defined by Equation 21 is in the use of inertial measurements rather than a vehicle dynamic model. Both approaches rely on numerically differentiating measurements of airspeed, but it is likely that measurements of acceleration will be more accurate than the predictions provided by a dynamic model.

Equations 22 and 27 together allow computation of the wind velocity (expressed in the inertial frame) and the wind acceleration as seen by the vehicle (expressed in the body frame). These can be used to compute velocity or trajectory commands for energy maximization or other tasks such as disturbance minimization. It is useful, however, to determine the expected error in wind field estimates.

III. Error Analysis

The wind field computation is subject to errors resulting from several sources, with two main sources being measurement error and errors in vehicle state estimates. This section discusses and quantifies the magnitudes of the wind field estimate errors as functions of the magnitude of the measurement and state errors.

A. Wind velocity estimation

While the computation above was done in terms of airspeed body components $u,\ v,\ w$, the results of the error analysis give intuitively more useful results when the wind computation is considered in terms of v_a, α and β. Assuming wings-level flight,

$$\begin{aligned} w_x &= \dot{x} - v_a \cos\gamma \cos\beta \cos\psi + v_a \cos\gamma \sin\beta \sin\psi && (28)\\ w_y &= \dot{y} - v_a \cos\gamma \cos\beta \sin\psi - v_a \cos\gamma \sin\beta \cos\psi && (29)\\ w_z &= \dot{z} - v_a \sin\gamma && (30) \end{aligned}$$

where $\gamma = \theta - \alpha$, the flight path angle with respect to the surrounding airmass.

Assuming that the errors in the measurements have a zero-mean Gaussian probability density, the error in the computed wind field can be determined by linearizing the equations above.

$$\begin{aligned} \mathbf{w} &= h(\mathbf{x}) \\ &\approx h(\bar{\mathbf{x}}) + \mathbf{H}(\mathbf{x} - \bar{\mathbf{x}}) && (31) \end{aligned}$$

where $\mathbf{H} = \nabla h$, the Jacobian of the wind computation equations with respect to the measurements. Assuming that the linearization of h is a good approximation over the range of uncertainty in $\mathbf{x}$, the error in estimated wind will have a zero-mean Gaussian probability density with covariance

$$\mathbf{\Sigma}_w = \mathbf{H}\mathbf{\Sigma}_x\mathbf{H}^T \quad (32)$$

where $\mathbf{\Sigma}_x$ is the covariance of the measurement noise. If the measurement noise is uncorrelated then

$$\mathbf{\Sigma}_x = \mathrm{diag}(\sigma_{\dot{x}}^2\ \sigma_{\dot{y}}^2\ \sigma_{\dot{z}}^2\ \sigma_{v_a}^2\ \sigma_\gamma^2\ \sigma_\beta^2\ \sigma_\psi^2) \quad (33)$$

where $\sigma_\gamma^2 = \sigma_\theta^2 + \sigma_\alpha^2$.

The components of the wind error covariance are

$$\begin{aligned} \Sigma_w(1,1) &= \sigma_{\dot{x}}^2 + \sigma_{v_a}^2 \cos^2\gamma \cos^2(\beta+\psi) + \sigma_\gamma^2 v_a^2 \sin^2\gamma \cos^2(\beta+\psi) \\ &\quad + (\sigma_\beta^2 + \sigma_\psi^2) v_a^2 \cos^2\gamma \sin^2(\beta+\psi) && (34)\\ \Sigma_w(1,2) &= \sigma_{v_a}^2 \cos^2\gamma \sin(\beta+\psi)\cos(\beta+\psi) + \sigma_\gamma^2 v_a^2 \sin^2\gamma \sin(\beta+\psi)\cos(\beta+\psi) \\ &\quad - (\sigma_\beta^2 + \sigma_\psi^2) v_a^2 \cos^2\gamma \sin(\beta+\psi)\cos(\beta+\psi) && (35)\\ \Sigma_w(1,3) &= -\sigma_{v_a}^2 \sin\gamma\cos\gamma\cos(\beta+\psi) + \sigma_\gamma^2 v_a^2 \sin\gamma\cos\gamma\cos(\beta+\psi) && (36)\\ \Sigma_w(2,2) &= \sigma_{\dot{y}}^2 + \sigma_{v_a}^2 \cos^2\gamma \sin^2(\beta+\psi) + \sigma_\gamma^2 v_a^2 \sin^2\gamma \sin^2(\beta+\psi) \\ &\quad + (\sigma_\beta^2 + \sigma_\psi^2) v_a^2 \cos^2\gamma \cos^2(\beta+\psi) && (37)\\ \Sigma_w(2,3) &= -\sigma_{v_a}^2 \sin\gamma\cos\gamma\sin(\beta+\psi) + \sigma_\gamma^2 v_a^2 \sin\gamma\cos\gamma\sin(\beta+\psi) && (38)\\ \Sigma_w(3,3) &= \sigma_{\dot{z}}^2 + \sigma_{v_a}^2 \sin^2\gamma + \sigma_\gamma^2 v_a^2 \cos^2\gamma && (39) \end{aligned}$$

The error covariance is symmetric, and off-diagonal terms represent correlation in the estimate error between components of the estimated wind. Correlation between the vertical and horizontal components (the 1,3 and 2,3 terms) can be removed by flying at $\gamma = 0$ (i.e. horizontal with respect to the surrounding airmass). Note that this is only possible during powered flight or during an unsteady glide: a steady, trimmed glide will always result in the aircraft descending in relation to the surrounding air mass. Correlation between horizontal components is removed by flying at $\beta + \psi = 0°,\ 90°,\ 180°,\ 270°$.

A measure of total error in the wind estimate is the trace of the covariance matrix:

$$\begin{aligned} e^2 &= \mathrm{Tr}\boldsymbol{\Sigma}_w \\ &= \sigma_{\dot{x}}^2 + \sigma_{\dot{y}}^2 + \sigma_{\dot{z}}^2 + \sigma_{v_a}^2 + \sigma_\gamma^2 v_a^2 + (\sigma_\beta^2 + \sigma_\psi^2) v_a^2 \cos^2\gamma \end{aligned} \tag{40}$$

Assuming that the flight path angle γ is small, minimizing the total error implies flying at low airspeed. Indeed, minimum error will result from flying at zero airspeed, i.e. using a neutrally buoyant balloon!

In practice the noise in the GPS velocity measurements will be correlated, but this will not affect the trace of the wind error covariance: it will add the GPS error correlation terms to the off-diagonal elements of $\boldsymbol{\Sigma}_w$.

When the flight path angle is small, $\cos^2\gamma \approx 1$ and

$$\begin{aligned} e^2 &= \sigma_{\dot{x}}^2 + \sigma_{\dot{y}}^2 + \sigma_{\dot{z}}^2 + \sigma_{v_a}^2 + v_a^2(\sigma_\gamma^2 + \sigma_\beta^2 + \sigma_\psi^2) \\ &= \sigma_{\dot{x}}^2 + \sigma_{\dot{y}}^2 + \sigma_{\dot{z}}^2 + \sigma_{v_a}^2 + v_a^2(\sigma_\theta^2 + \sigma_\alpha^2 + \sigma_\beta^2 + \sigma_\psi^2) \end{aligned} \tag{41}$$

Since $\gamma = \theta - \alpha$, $\sigma_\gamma^2 = \sigma_\theta^2 + \sigma_\alpha^2$.

For unaided GPS the standard deviation of the velocity error is approximately 0.1 m/s. This can be reduced with carrier phase differential GPS to order mm/s. Assuming that airspeed can be measured to an accuracy of 0.2 m/s (0.4 knot) and angles can be measured to an accuracy of 1° the unaided value of estimation error is approximately $e^2 = 0.07 + 0.0012 v_a^2$. Under these conditions the angle-related errors equal the speed-measurement errors when airspeed is 7.58 m/s, and the total expected error at this speed is 0.37 m/s. When airspeed is 16 m/s the expected error in computed wind speed is $e = 0.61$m/s. If carrier phase differential GPS is used (assuming velocity error is 5 mm/s) the expected error is $e^2 = 0.0401 + 0.0012 v_a^2$, leading to a predicted error of 0.59 m/s. This improvement is not significant: critical parameters in reducing wind speed estimate errors are the noise in measurements of airspeed and angles and flying at low airspeed.

B. Rate of change of wind velocity estimation

The Jacobian of $\dot{\mathbf{w}}$ with respect to measurements and states is obtained from Equation 27:

$$\mathbf{H}_{\dot{\mathbf{W}}} = \begin{bmatrix} 1 & 0 & 0 & 0 & -g\cos\theta & -\frac{1}{\Delta t} & r & -q & 0 & -w & v \\ 0 & 1 & 0 & g\cos\theta\cos\phi & -g\sin\theta\sin\phi & r & -\frac{1}{\Delta t} & -p & -w & 0 & u \\ 0 & 0 & 1 & -g\cos\theta\sin\phi & -g\sin\theta\cos\phi & -q & p & -\frac{1}{\Delta t} & v & -u & 0 \end{bmatrix} \tag{42}$$

The covariance of the expected error in the wind acceleration estimate is

$$\boldsymbol{\Sigma}_{\dot{w}} = \mathbf{H}_{\dot{\mathbf{W}}} \boldsymbol{\Sigma}_x \mathbf{H}_{\dot{\mathbf{W}}}^T \tag{43}$$

where (for uncorrelated measurement noise),

$$\boldsymbol{\Sigma}_x = \mathrm{diag}(\sigma_{a_x}^2\ \sigma_{a_y}^2\ \sigma_{a_z}^2\ \sigma_{phi}^2\ \sigma_{theta}^2\ \sigma_u^2\ \sigma_v^2\ \sigma_w^2\ \sigma_p^2\ \sigma_q^2\ \sigma_r^2\ ) \tag{44}$$

The square of the magnitude of the expected error is the trace of the covariance matrix:

$$\begin{aligned} e_{\dot{w}}^2 &= \mathrm{Tr}\boldsymbol{\Sigma}_{\dot{w}} \\ &= \sigma_{a_x}^2 + \sigma_{a_y}^2 + \sigma_{a_z}^2 + g^2\cos^2\theta\sigma_\phi^2 + g^2\sigma_\theta^2 \\ &\quad + \left(\frac{1}{\Delta t^2} + r^2 + q^2\right)\sigma_u^2 + \left(\frac{1}{\Delta t^2} + r^2 + p^2\right)\sigma_v^2 + \left(\frac{1}{\Delta t^2} + p^2 + q^2\right)\sigma_w^2 \\ &\quad + \left(w^2 + v^2\right)\sigma_p^2 + \left(w^2 + u^2\right)\sigma_q^2 + \left(u^2 + v^2\right)\sigma_r^2 \end{aligned} \tag{45}$$

A major contributor to error is the numerical differentiation of the airspeed measurements (reflected in the $\frac{\sigma_{(u,v,w)}^2}{\Delta t^2}$ terms). The contribution of noise in angular rate measurements can be reduced by flying at low airspeed. Noise in the pitch and bank angles result in uncertainty of the projection of gravity into the body frame.

C. Smoothing/filtering the estimates

It is clear that estimates of wind speed and wind acceleration can be quite noisy. One approach to reducing noise is a smoothing filter such as a moving average. Clearly filter length must be chosen carefully to reduce noise without causing too much lag in the estimates. Hand tuning found that a ten step moving average significantly reduced noise in the wind estimates without greatly affecting lag.

IV. Simulation and Discussion

To assess the effectiveness of the proposed approach both three and six degree of freedom simulations were conducted. The aircraft model is a small autonomous glider flying at approximately 16 m/s. A state feedback controller regulates states to maintain trimmed flight at best L/D. Note that the only control input is elevator deflection. An on-board autopilot module is assumed to provide measurements of position and Earth-relative velocity via GPS and estimates of airspeed and orientation. Measurements of body angular rates are provided by the autopilot module via its rate gyros. Assumed measurement noise and estimate uncertainties are given in Table 1. The autopilot is assumed to provide this data at a rate of 50 Hz. Under the conditions defined in Table 1 the expected error in wind velocity estimation at 16 m/s airspeed is 0.37 m/s for three degree of freedom simulations and 0.46 m/s for six degree of freedom simulations (Equation 41).

Table 1. Measurement noise and estimate uncertainties for simulations.

parameter	source	variable	1σ noise/uncertainty
position	GPS measurement via autopilot	$x,\ y,\ z$	3 m
orientation	state estimate from autopilot	$\phi,\ \theta,\ \psi$	$\sigma_\phi = \sigma_\psi = 0,\ \sigma_\theta = 1^\circ$
airspeed	state estimate from autopilot	$u,\ v,\ w$	$\sigma_u = 0.2$ m/s, $\sigma_v = \sigma_w = 0.05$ m/s
ground speed	GPS measurement via autopilot	$\dot{x},\ \dot{y},\ \dot{z}$	0.1 m/s
acceleration	IMU measurement via autopilot	$a_{x,b},\ a_{y,b},\ a_{z,b}$	0.1 m/s^2
angular rate	IMU measurement via autopilot	$p,\ q,\ r$	0.1 rad/s

A. Gust field definition

Gust fields are modeled using a frozen Dryden turbulence model. Airmass motion is thus represented as a sum of sinusoids:

$$w_{(\cdot)} = w_{(\cdot),0} + \sum_{n=1}^{N} a_{(\cdot),n} \sin\left(\Omega_{(\cdot),n} s + \phi_{(\cdot),n}\right) \tag{46}$$

where $(\cdot)$ denotes a component (either u or w for longitudinal or vertical gusts, respectively) and s is motion along the flight path. Random values of $\phi_{(\cdot),n}$ simulate the random process and the choice of coefficients $a_{(\cdot),n}$ defines the power spectral density. For a Dryden gust field the power spectral density is defined as

$$\Phi_u(\Omega) = \sigma_u^2 \frac{2L_u}{\pi} \frac{1}{1 + (L_u\Omega)^2} \tag{47}$$

$$\Phi_w(\Omega) = \sigma_w^2 \frac{L_w}{\pi} \frac{1 + 3(L_w\Omega)^2}{(1 + (L_w\Omega)^2)^2} \tag{48}$$

For low altitudes (below 1000 feet), the length scale of the vertical gust is $L_w = h$ and the turbulence intensity is $\sigma_w = 0.1 w_{20}$, where w_{20} is the wind speed at 20 feet altitude. Horizontal gust length scale and intensity are related to the vertical gust scale and intensity by

$$\frac{L_u}{L_w} = \frac{1}{(0.177 + 0.000823h)^{1.2}} \tag{49}$$

$$\frac{\sigma_u}{\sigma_w} = \frac{1}{(0.177 + 0.000823h)^{0.4}} \tag{50}$$

where h is in feet.

The amplitude of a sinusoid in Equation 46 is computed as[18]

$$a_n = \sqrt{\Delta\Omega_n \Phi(\Omega_n)} \tag{51}$$

Note that a sinusoidal gust field is represented by setting $N = 1$ and defining the amplitude at the desired frequency.

B. Dryden gust fields

Three degree of freedom simulations of flight through Dryden gust fields at an altitude of 50 meters and $w_{20} = 10$ m/s were conducted to assess overall performance. A 500 run Monte Carlo simulation compares the predicted error with the actual error. Each run consists of a sixty second flight through a Dryden gust field, a new gust field was generated for each run.

Results of wind velocity estimation are shown in Figure 2. Detailed results of a single run (zoomed in to show a single wavelength of the x-component of wind) are shown in subplot (a). The upper two plots of Figure 2(a) show x and z components of wind field, estimated wind field, and smoothed estimated wind field. The lower plot shows the 2-norm of the error along with the expected error. For this run the airspeed varies by about 1.5m/s, not enough to have a significant influence on the estimation error. The green line shows the effect of smoothing on the estimated wind speed.

Figure 2(b) shows overall results of the Monte Carlo simulation. Maximum error did not exceed 1.5 m/s, with the mean error of 0.33 m/s closely matching the predicted mean error of 0.37 m/s. Smoothing using a 10 step moving average reduced the mean error to 0.22 m/s.

Results of wind acceleration estimation are shown in Figure 3. Detailed results of a single run (zoomed in to show a single wavelength of the x-component of wind) are shown in subplot (a). The error in x-component of wind acceleration is significantly larger than the z component. Expanding Equation 43, and assuming longitudinal motion, the variance of the error in x and z components of wind acceleration are

$$\Sigma_{\dot{\mathbf{w}},xx} = \sigma_{a_x}^2 + g^2\sigma_\theta^2 \cos^2\theta + \frac{1}{\Delta t^2}\sigma_u^2 + q^2\sigma_w^2 + w^2\sigma_q^2 \tag{52}$$

$$\Sigma_{\dot{\mathbf{w}},zz} = \sigma_{a_z}^2 + g^2\sigma_\theta^2 \sin^2\theta + \frac{1}{\Delta t^2}\sigma_w^2 + q^2\sigma_u^2 + u^2\sigma_q^2 \tag{53}$$

These simulations have defined σ_u four times larger that σ_w, hence the standard deviation of the error in x acceleration estimates will be roughly four times larger than the w acceleration estimates.

Figure 3(b) shows the envelope of the 2-norm of the acceleration estimate error, the mean acceleration error and the predicted acceleration error. The mean true error was 8.6 m/s^2, predicted error was 10.0 m/s^2. Smoothing reduced error to 4.33 m/s^2 at a cost of reducing the ability to follow changes in acceleration. An improved model for airspeed measurements would greatly improve estimation of wind acceleration.

C. Sinusoidal gust fields

Six degree of freedom simulated flights through noisy sinusoidal gust fields were conducted for ease of visualization of results and to assess the error in wind estimation.

Results of wind velocity estimation are shown in Figure 4. Detailed results of a single run are shown in subplot (a). The upper three plots of Figure 4(a) show x, y, and z components of wind field, estimated wind field, and smoothed estimated wind field. The lower plot shows the 2-norm of the error along with the expected error. For this run the airspeed varies from 13.5 m/s to 19.5 m/s roughly in phase with increasing headwind (negative values of w_x) and this is enough that the effect of airspeed on estimation error can be seen. Increasing airspeed corresponds to increasing error in the estimated wind field, as predicted. The green line shows the effect of smoothing on the estimated wind speed.

Figure 4(b) shows overall results of the Monte Carlo simulation. Maximum error did not exceed 1.5 m/s, with the mean error of 0.45 m/s closely matching the predicted mean error of 0.46 m/s.

Results of wind acceleration estimation are shown in Figure 5. Detailed results of a single run are shown in subplot (a). The upper three plots of Figure 5(a) show x, y, and z components of wind acceleration, estimated wind acceleration, and smoothed estimated wind acceleration. The lower plot shows the 2-norm of the error along with the expected error. Not surprisingly estimates of wind acceleration are very noisy (due to the numerical differentiation of the airspeed measurement). Since the largest contributor to error is the numerical differentiation, the expected error is essentially constant at 13.8 m/s^2.

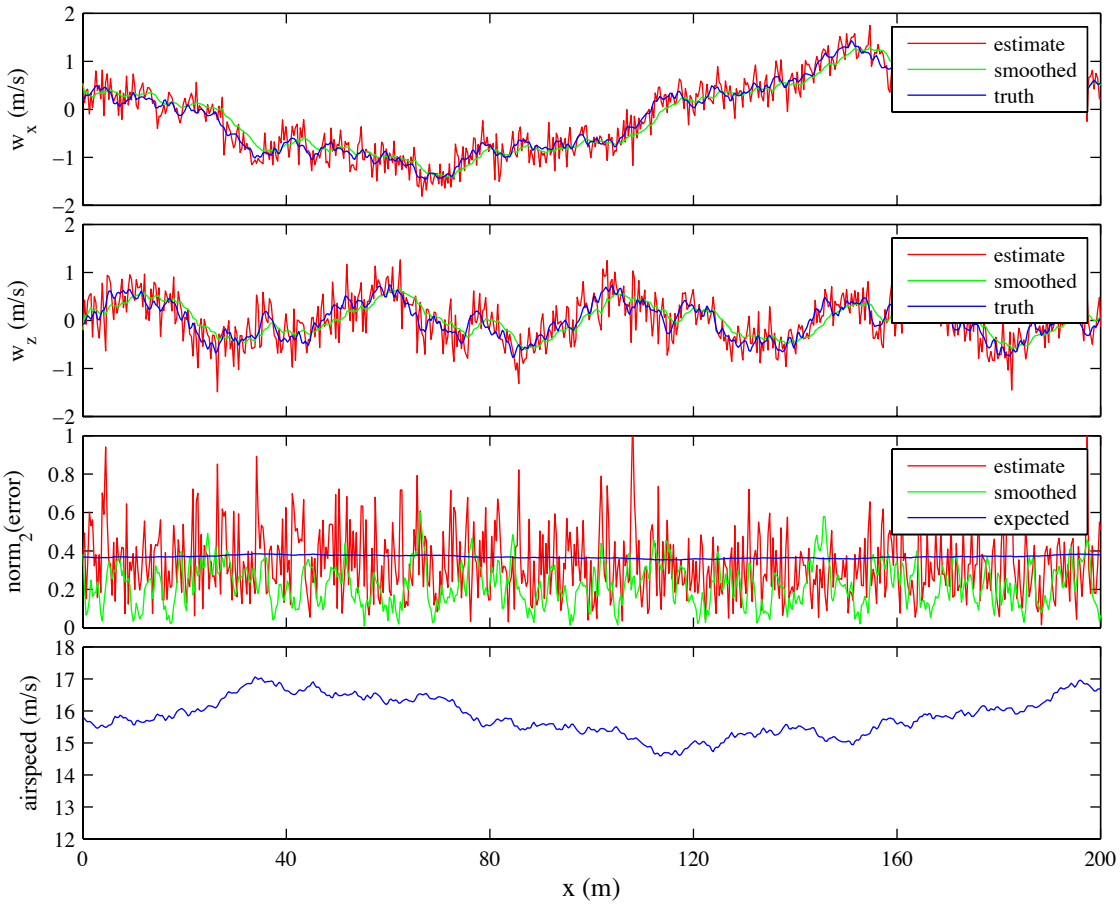

(a) Detail of one run

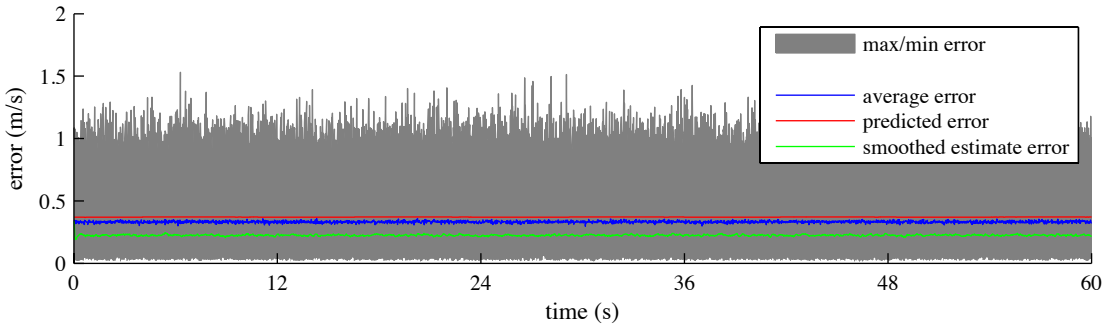

(b) Monte Carlo simulation results

Figure 2. Wind velocity estimation for 3DOF Dryden wind field. Subplot (a): The top two plots show components of the wind field (estimated in red, smoothed estimated in green, and truth in blue), the third plot shows the 2-norm of the estimate error for a single run, and the bottom plot shows airspeed. Subplot (b): Monte Carlo simulation of wind field estimation: 2-norm of error in velocity estimate. Maximum and minimum errors shown by grey envelope, average error at each time step shown in blue, predicted error shown in red, average smoothed error shown in green.

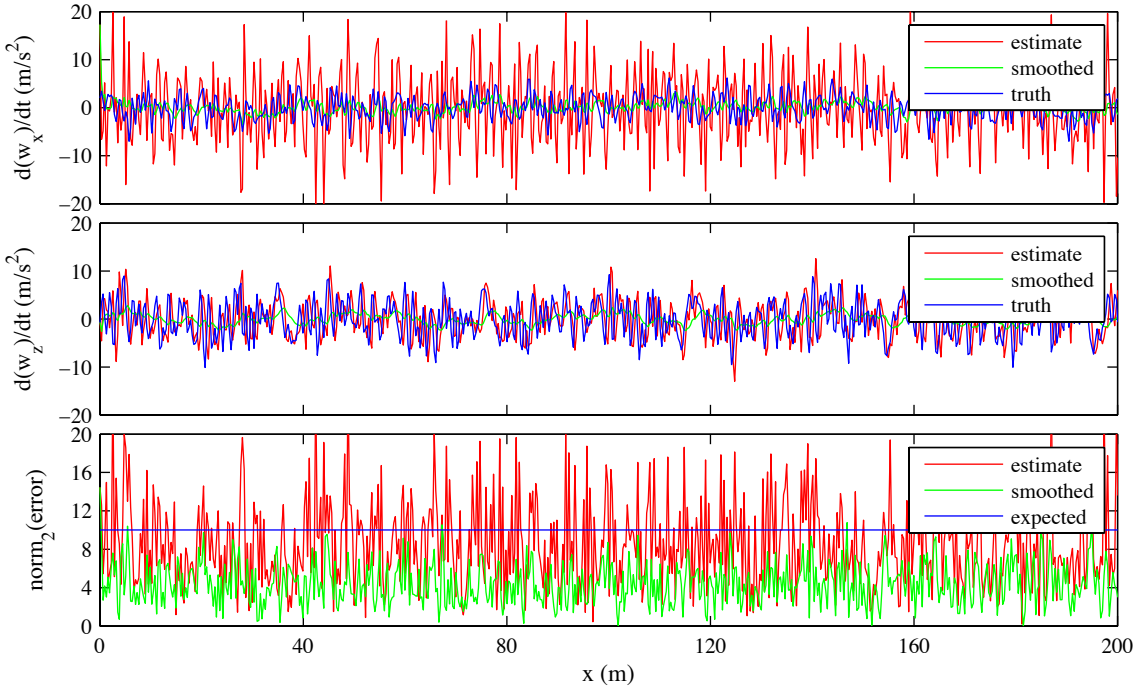

(a) Detail of one run

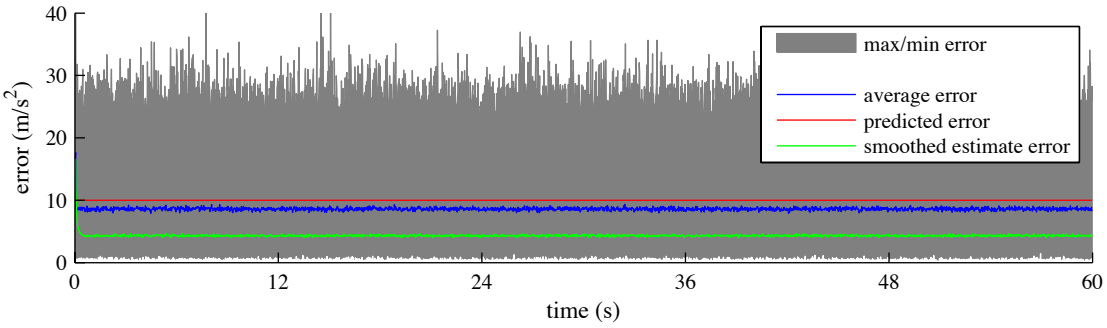

(b) Monte Carlo simulation results

Figure 3. Wind acceleration estimation for 3DOF Dryden wind field. Subplot (a): The top two plots show components of the wind acceleration (estimated in red, smoothed estimated in green, and truth in blue), the bottom plot shows the 2-norm of the estimate error for a single run. Subplot (b): Monte Carlo simulation of wind acceleration estimation: 2-norm of error in velocity estimate. Maximum and minimum errors shown by grey envelope, average error at each time step shown in blue, predicted error shown in red, average smoothed error shown in green.

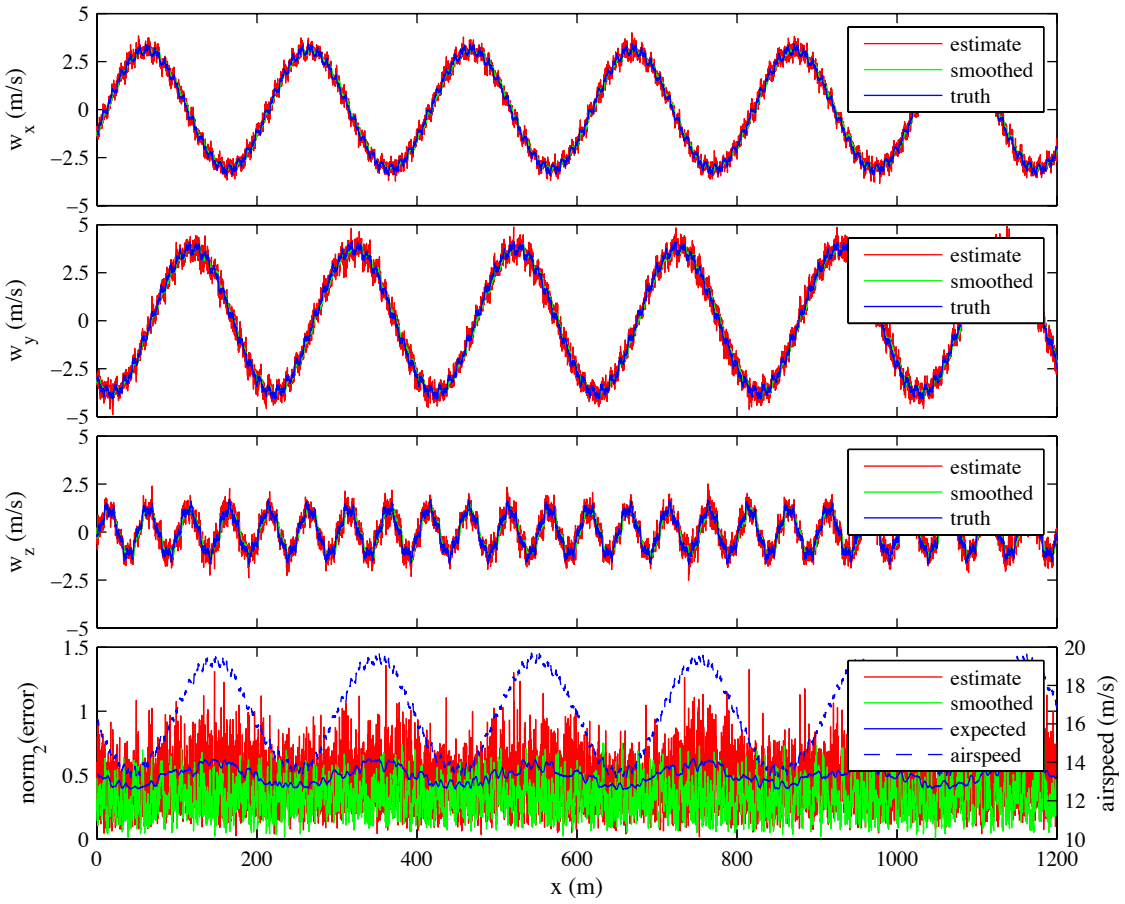

(a) detail

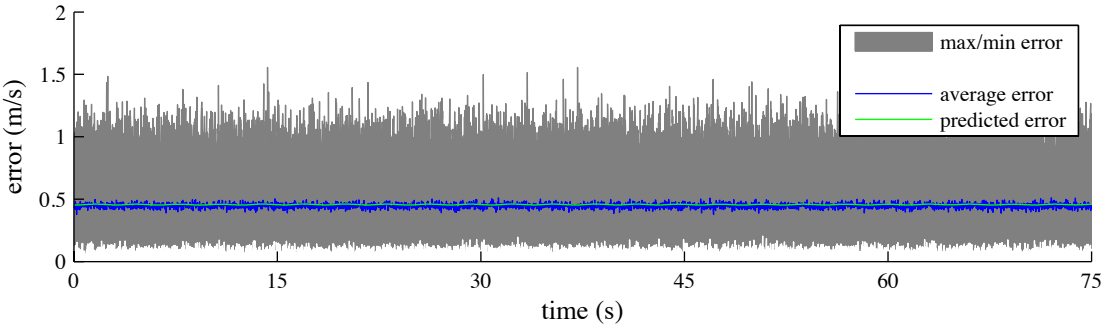

(b) Monte Carlo simulations

Figure 4. 6DOF wind velocity estimation for noisy sinusoidal wind field. Plot (a): The top three plots show components of the wind field, the bottom plot shows the 2-norm of the estimate error. Plot (b): Monte Carlo simulation of wind field estimation: 2-norm of error in velocity estimate. Maximum and minimum errors shown by grey envelope, average error at each time step shown in blue, predicted error shown in green.

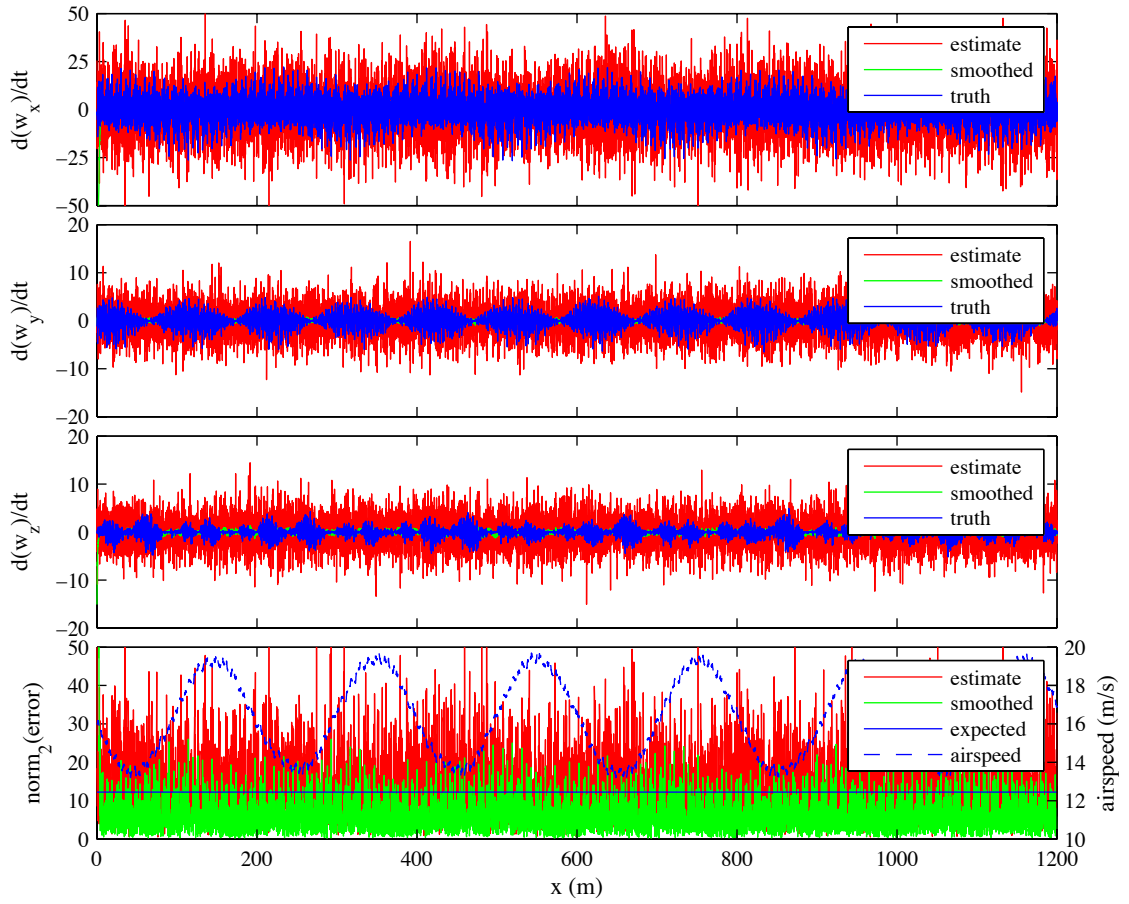

(a) detail

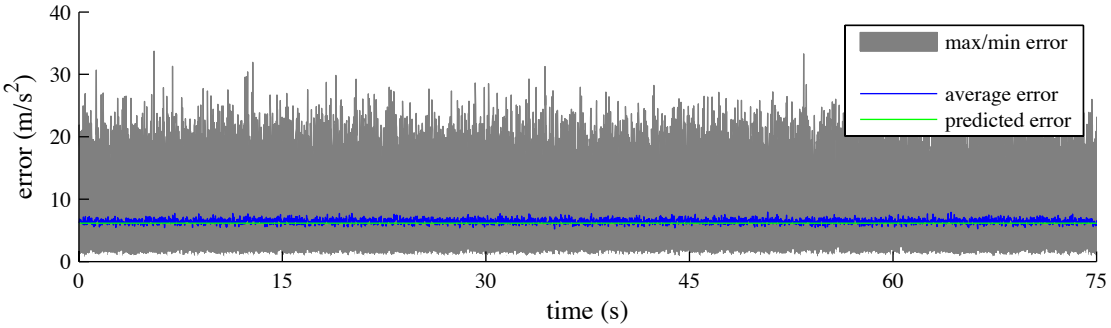

(b) Monte Carlo simulations

Figure 5. 6DOF wind acceleration estimation for noisy sinusoidal wind field. Plot (a): The top three plots show components of the wind field, the bottom plot shows the 2-norm of the estimate error. Plot (b): Monte Carlo simulation of wind field estimation: 2-norm of error in acceleration estimate. Maximum and minimum errors shown by grey envelope, average error at each time step shown in blue, predicted error shown in green.

Figure 5(b) shows overall results of a Monte Carlo simulation. For the Monte Carlo simulation the time step was set to 0.02s, double the value for the detailed plot. The mean error is therefor half the value of the error in the detailed plot. The predicted mean error and the true mean error match very closely.

V. Wind estimation and energy harvesting

Since earlier research has shown that energy harvesting from gusts is feasible when wind is known, an important question is the feasibility of of energy harvesting when wind is not known. Simulations of longitudinal energy harvesting using a slight modification of a previously developed gust soaring control architecture along with the wind estimation algorithm presented here are discussed.

This architecture is shown in Figure 6. In brief, measurements of airspeed, GPS velocity, orientation, acceleration and angular rate are used to estimate the wind field. The components of wind speed are used to compute a state which maximizes the change in energy per unit of distance travelled, and a closed-loop controller attempts to follow these state commands. Here the closed-loop control law is computed using LQR synthesis, with vehicle dynamics linearized about steady trimmed flight at best L/D.[19]

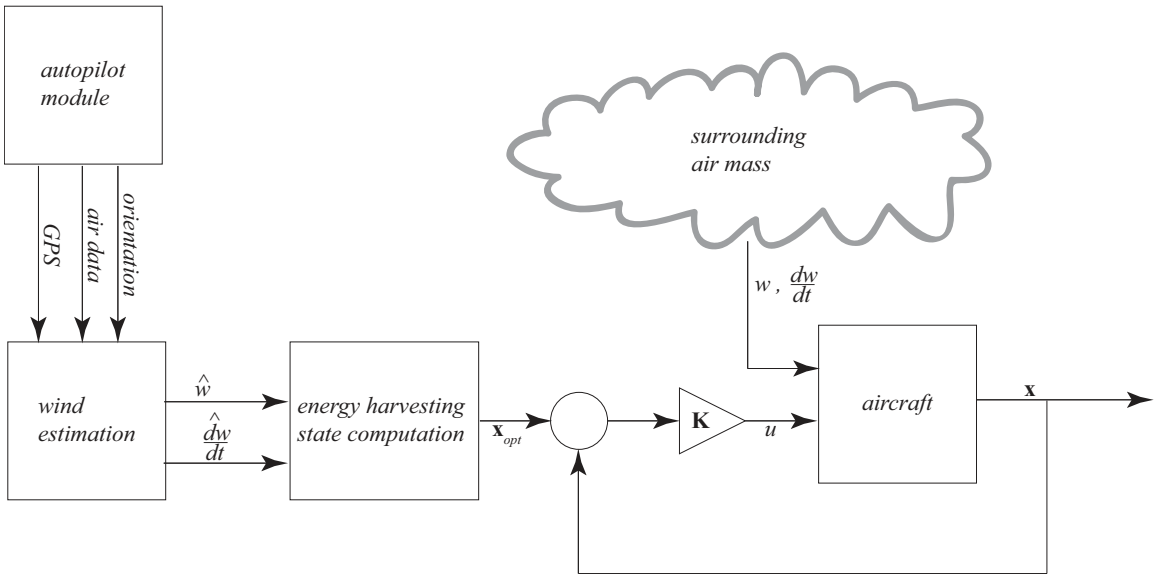

Figure 6. Atmospheric energy harvesting system using estimates of wind.

There is an important difference in the speed computation used here and that described earlier: wind gradients are not included in the computation of speed to fly. A brief investigation (not discussed here) showed that including wind gradients in the energy harvesting state computation for gust fields involving longitudinal as well as vertical gusts did not provide as large a performance gain as it did in fields involving only vertical gusts (even when winds were assumed known). This may be due to an incorrect choice of weight matrices $\mathbf{Q}$ and $\mathbf{R}$ in the LQR synthesis (matrices computed in earlier work for vertical-only gusts were used here, rather than computing new values including the effects of longitudinal gusts[19]). However, this requires further investigation.

The vehicle considered is the RnR Products SB-XC, a 4.3m wingspan aircraft. Parameters are given in Table 3 and control saturation and state limits are given in Table 4. The controller gain used for all cases was[19]

$$\mathbf{K} = \begin{bmatrix} 1.0106 & -0.0277 & 5.8082 & 0.5847 \end{bmatrix} \tag{54}$$

Simulation results flights through four turbulence conditions are presented: low altitude, light turbulence; low altitude, moderate turbulence; medium altitude, light turbulence; finally medium altitude, moderate turbulence. Properties of the gust fields are defined by MIL-F-8785C and are summarized in Table 2. Note that medium altitude gust fields are isotropic, while at low altitude (below 1000 feet) both gust intensity and the fundamental length depends on direction. For each case a Monte Carlo simulation of 50 runs was performed to assess flight performance using four controllers: (1) constant airspeed flight controller; (2) the

gust energy harvesting controller assuming known wind conditions; (3) the gust energy harvesting controller using estimated wind conditions; (4) finally the gust energy harvesting controller using smoothed estimates. The constant speed flight controller uses the same gain matrix computed for gust energy harvesting, however rather than attempting to follow state commands for optimal energy harvesting it tracks the state which defines a trimmed glide at best L/D in still air ($v_a = 15.8$ m/s, $\theta = 0.7°$, $\alpha = 2.8°$).

Each run consisted of 8 minutes simulated flight through the gust field, resulting in approximately 7600m distance flown for each run. A new random gust field was generated for each of the 50 runs.

Table 2. Gust field properties.

description	altitude (m)	L_u (m)	L_w (m)	σ_u (m/s)	σ_w (m/s)
low altitude, light turbulence	50	200	50	1.06	0.7
low altitude, moderate turbulence	50	200	50	2.12	1.4
medium altitude, light turbulence	600	533	533	1.5	1.5
medium altitude, moderate turbulence	600	533	533	3.0	3.0

Results of all cases are summarized in Figure 7. Subfigure (a) shows maximum, minimum, mean, and 1σ values of $\frac{\Delta e_{tot}}{\Delta x}$ (i.e. change in total energy over distance flown) for each control case over the 50 runs in each turbulence case. The lower plot of Subfigure 7(a) shows the average (over all runs) of the root mean square elevator deflection for each controller (a measure of the amount of control required).

The difference in energy harvesting using known versus estimated wind is slight (the plots lie essentially on top of each other). Steadily increasing improvement over the baseline (constant speed) case is visible. In fact the medium altitude cases show that many of the gust fields actually result in net energy gain.

However, a clear difference is visible in the root mean square elevator deflection, with the use of wind estimates greatly increasing required control (Figure 7(a), lower plot). Using smoothed wind estimates reduces root mean square elevator deflection to the level observed for energy harvesting using known wind; however it does not significantly reduce the energy harvested.

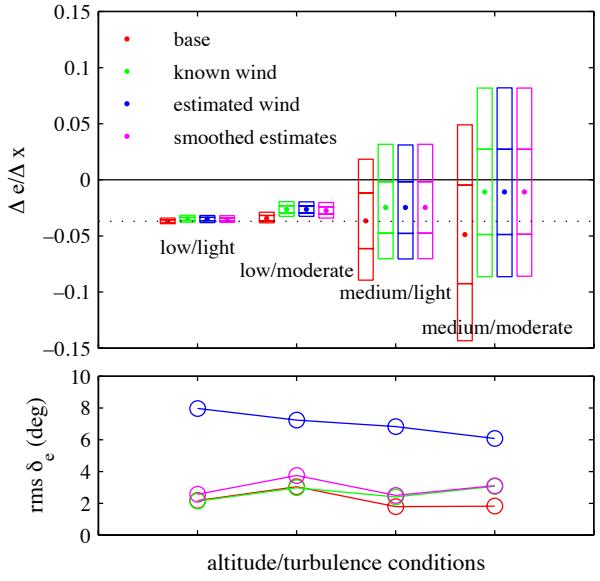

(a) energy change and control effort

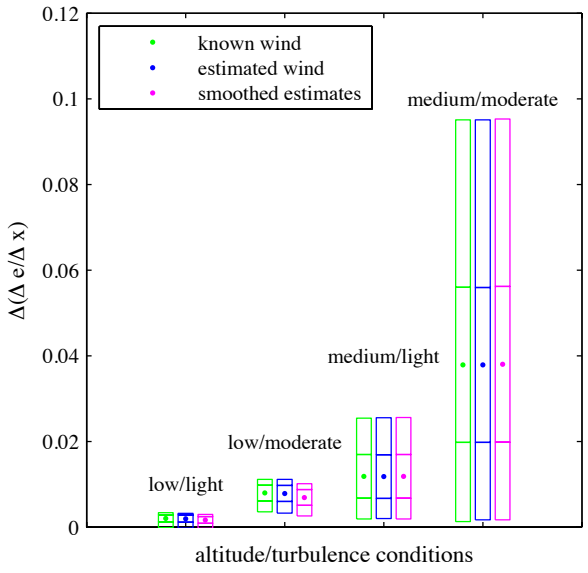

(b) improvement in energy change over baseline

Figure 7. Summary of energy harvesting using estimated winds for all turbulence conditions. Subplot (a) shows energy change per distance flown for each case and control effort; subplot (b) shows the improvement in flight performance over the baseline (constant speed) controller. The bars show minimum, maximum and 1σ, the dots show mean values (over the 50 runs in each Monte Carlo simulation). The dotted black line in the upper plot of subfigure (a) shows $\frac{de}{dx}$ for a steady glide at best L/D in still air.

The difference in energy change between the energy harvesting controller and a constant airspeed controller is showing in Figure 7(b). The gust energy harvesting controller shows better performance for all runs, with the level of improvement increasing as the turbulence intensity increases.

Detailed results for each turbulence condition are shown in Figures 8 through 11.

A general conclusion is that the constant speed controller flies too slowly in regions of unfavorable wind (downwards or headwind) and too fast in regions of favorable wind (upwards or tailwind). Thus too much time is spent in unfavorable conditions and not enough time is spent in favorable conditions. This is magnified in the medium altitude cases, where the length scale of turbulence is larger. Second, significantly more elevator deflection is required at lower altitudes for all controllers. This is most likely due to the shorter scales of turbulence.

VI. Conclusion

A method for estimating dynamic three dimensional wind fields using a sensor suite typical of small unmanned aerial vehicles has been presented. Analysis of the predicted error shows that the error in wind velocity estimates is dependent on vehicle airspeed and the error in wind acceleration is due in large part to noise in measurements of airspeed. Results of Monte Carlo simulations agree very closely with the predicted errors.

Simulations using realistic levels of noise and uncertainty show that wind velocity can be estimated to an accuracy of better than 0.5 m/s. Since the earth-relative velocity of the vehicle can be measured quite accurately using GPS, the key to reducing this error further is increasing the accuracy of airspeed measurements and increasing the accuracy of vehicle orientation measurements.

Simulations combining this wind field estimation algorithm with a gust energy harvesting controller showed that efficient energy harvesting is still possible. The cost of using wind estimates lies in significantly increased control actuation, but this can be greatly reduced by smoothing the estimates using a moving average filter. This smoothing filter reduced control actuation to the level observed for flight through *a priori* known wind fields without significant effect on energy harvesting.

Acknowledgments

This research was funded by the Office of Naval Research under Contract Number N00014-09-M-0307. The authors also thank Dan Kuehme for assistance in running simulations.

References

[1]Rayleigh, J. W. S., "The Soaring of Birds," *Nature*, Vol. 27, 1883, pp. 534–535.

[2]Rayleigh, J. W. S., "The Sailing Flight of the Albatross," *Nature*, Vol. 40, 1889, pp. 34.

[3]Pennycuick, C. J., "Gust Soaring as a Basis for the Flight of Petrels and Albatrosses (Procellariiformes)," *Avian Science*, Vol. 2, No. 1, 2002, pp. 1–12.

[4]Sachs, G., "Minimum Shear Wind Strength Required for Dynamic Soaring of Albatrosses," *Ibis*, Vol. 147, 2005, pp. 1–10.

[5]Lissaman, P. B. S. and Patel, C. K., "Neutral Energy Cycles for a Vehicle in Sinusoidal and Turbulent Vertical Gusts," *45th AIAA Aerospace Sciences Meeting and Exhibit*, AIAA Paper 2007-863, American Institute of Aeronautics and Astronautics, Reno, Nevada, January 2007.

[6]Qi, Y. C. and Zhao, Y. J., "Energy-Efficient Trajectories of Unmanned Aerial Vehicles Flying Through Thermals," *Journal of Aerospace Engineering*, Vol. 18, No. 2, April 2005, pp. 84–92.

[7]Langelaan, J. W. and Bramesfeld, G., "Gust Energy Extraction for Mini- and Micro- Uninhabited Aerial Vehicles," *46th AIAA Aerospace Sciences Meeting and Exhibit*, AIAA Paper 2008-0223, American Institute of Aeronautics and Astronautics, Reston, Virginia, January 2008.

[8]Patel, C. K., *Energy Extraction from Atmospheric Turbulence to Improve Aircraft Performance*, VDM Verlag Dr. Müller, Saarbrüken, 2008.

[9]Watkins, S., Milbank, J., and Loxton, B. J., "Atmospheric Winds and the Implications for Microair Vehicles," *AIAA Journal*, Vol. 44, No. 11, November 2006, pp. 2591–2600.

[10]Pachter, M., Ceccarelli, N., and Chandler, P. R., "Estimating MAV's Heading and the Wind Speed and Direction using GPS, Inertial and Air Speed Measurements," *AIAA Guidance, Navigation and Control Conference*, AIAA Paper 2008-6311, American Institute of Aeronautics and Astronautics, Reston, Virginia, August 2008.

[11]Rodriguez, A. F., Andersen, E., Bradley, J. F., and Taylor, C. N., "Wind Estimation using an Optical Flow Sensor on a Miniature Air Vehicle," *AIAA Guidance, Navigation and Control Conference*, AIAA Paper 2007-6614, American Institute of Aeronautics and Astronautics, Reston, Virginia, August 2007.

[12]Myschik, S., Heller, M., Holzapfel, F., and Sachs, G., "Low-cost Wind Measurement System for Small Aircraft," *AIAA*

Guidance, Navigation and Control Conference, AIAA Paper 2004-5240, American Institute of Aeronautics and Astronautics, Reston, Virginia, August 2004.

[13]Myschik, S. and Sachs, G., "Flight Testing an Integrated Wind/Airdata and Navigation System for General Aviation Aircraft," *AIAA Guidance, Navigation and Control Conference*, AIAA Paper 2007-6796, American Institute of Aeronautics and Astronautics, Reston, Virginia, August 2007.

[14]de Divitiis, N., "Wind Estimation on a Lightweight Vertical Takeoff and Landing Uninhabited Vehicle," *Journal of Aircraft*, Vol. 40, No. 4, July-August 2003, pp. 759–767.

[15]Military Specification, "Flying Qualities of Piloted Airplanes," Tech. Rep. MIL-F-8785C, November 1980.

[16]Etkin, B. and Reid, L. D., *Dynamics of Flight: Stability and Control*, John Wiley & Sons, New York, 3rd ed., 1996.

[17]Misra, P. and Enge, P., *Global Positioning System: Signals, Measurements and Performance*, Ganga-Jamuna Press, Lincoln, Massachusetts, 2nd ed., 2006.

[18]Hoblit, F. M., *Gust Loads on Aircraft: Concepts and Applications*, AIAA Education Series, American Institute of Aeronautics and Astronautics, Reston, Virginia, 1988.

[19]Langelaan, J. W., "Gust Energy Extraction for Mini- and Micro- Uninhabited Aerial Vehicles," *Journal of Guidance, Control and Dynamics*, Vol. 32, No. 2, March-April 2009, pp. 464–473.

Appendix: Vehicle Properties

Table 3. Parameters for SB-XC glider.

variable	value	description
m	10 kg	mass
b	4.34 m	span
c	0.232 m	MAC
S	1 m^2	wing area
I_{yy}	1.87 kg.m^2	pitch moment of inertia
C_{L0}	0.37	
C_{L_α}	5.54 /rad	
C_{L_Q}	-3.255 s/rad	
$C_{L_{\dot\alpha}}$	-0.651 s/rad	
$C_{L_{\delta_e}}$	-0.37 /rad	
$C_{L_{\delta_f}}$	1.63 /rad	
$f_{LD}(\varphi)$	$0.1723\varphi^4 - 0.3161\varphi^3 + 0.2397\varphi^2$ $-0.0624\varphi + 0.0194$	$\varphi = C_{L0} + C_{L_\alpha}\alpha$
$C_{D_{\delta_e}}$	0 /rad	
$C_{D_{\delta_f}}$	0.042 /rad	
C_{m0}	0	
C_{m_α}	-1.02 /rad	
C_{m_Q}	-14.6 s/rad	
$C_{m_{\delta_e}}$	1.6275 /rad	
$C_{m_{\delta_f}}$	-0.254 /rad	

Table 4. State limits and control saturation for SB-XC glider.

state/control	range	description
θ	$[-45°\ 45°]$	pitch
v_a	[11m/s 35m/s]	airspeed
α	$[-2°\ 12°]$	angle of attack
Q	[−999 999]	pitch rate
δ_e	$[-20°\ 20°]$	elevator deflection

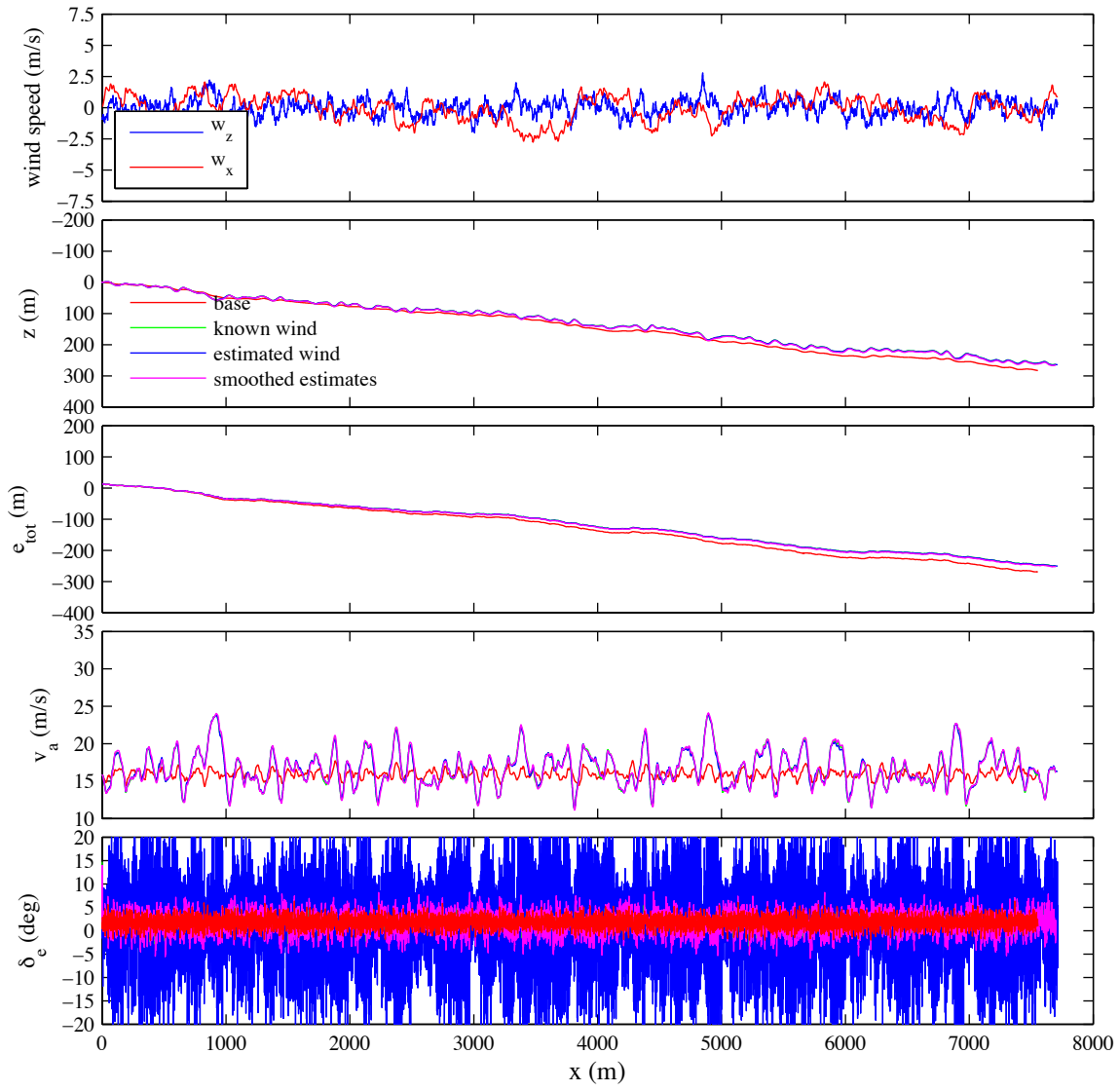

(a) Single run detail

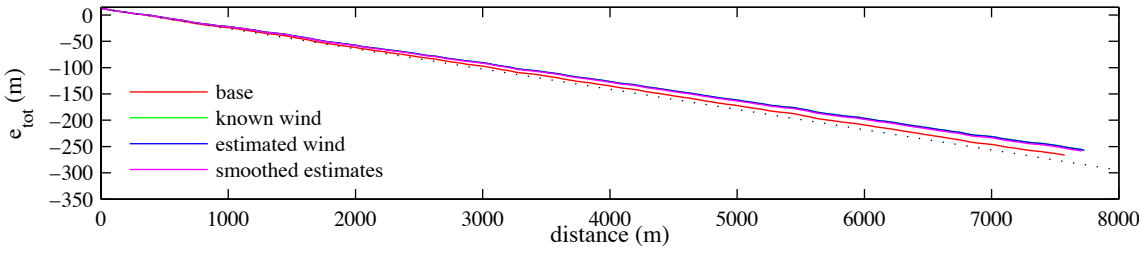

(b) Mean total energy

Figure 8. Performance comparison for flight through Dryden turbulence, low altitude, light intensity. Baseline (constant airspeed) control shown in red; energy harvesting control with known wind shown in green; energy harvesting control with estimated wind shown in blue; energy harvesting control using smoothed estimates shown in magenta. Subplot (a): upper plot shows true wind field (ix in red, iz in blue); second plot shows flight path; third shows total energy; fourth shows airspeed; fifth (bottom) shows elevator deflection; Subplot (b): mean value of total energy vs. distance over all runs. The dotted black line shows total energy change versus distance for a steady glide in zero wind.

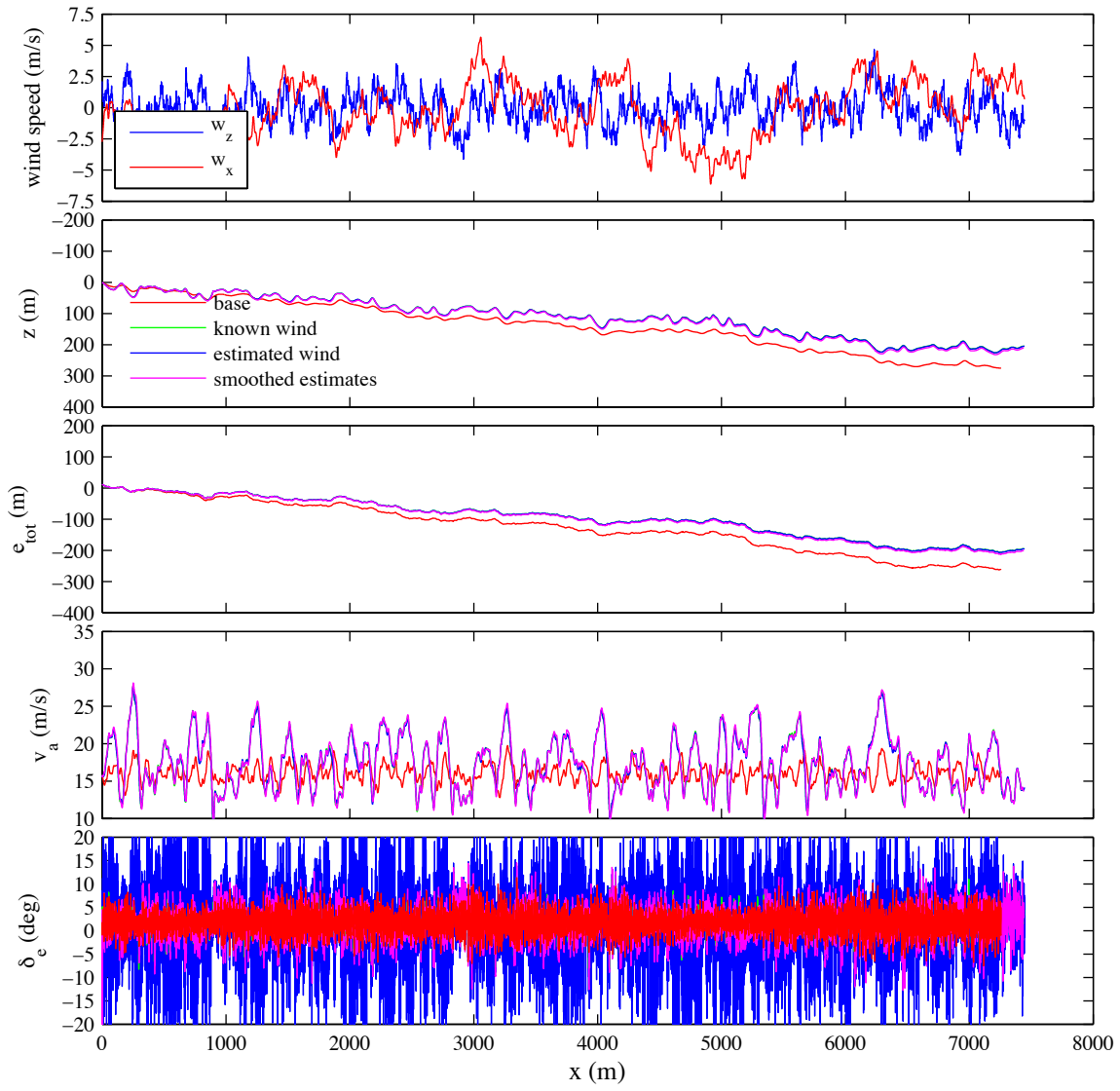

(a) Single run detail

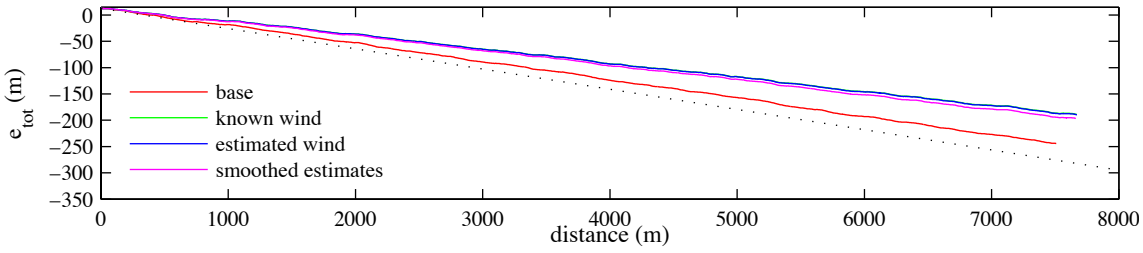

(b) Mean total energy

Figure 9. Performance comparison for flight through Dryden turbulence, low altitude, moderate intensity. Baseline (constant airspeed) control shown in red; energy harvesting control with known wind shown in green; energy harvesting control with estimated wind shown in blue; energy harvesting control using smoothed estimates shown in magenta. Subplot (a): upper plot shows true wind field (ix in red, iz in blue); second plot shows flight path; third shows total energy; fourth shows airspeed; fifth (bottom) shows elevator deflection; Subplot (b): mean value of total energy vs. distance over all runs. The dotted black line shows total energy change versus distance for a steady glide in zero wind.

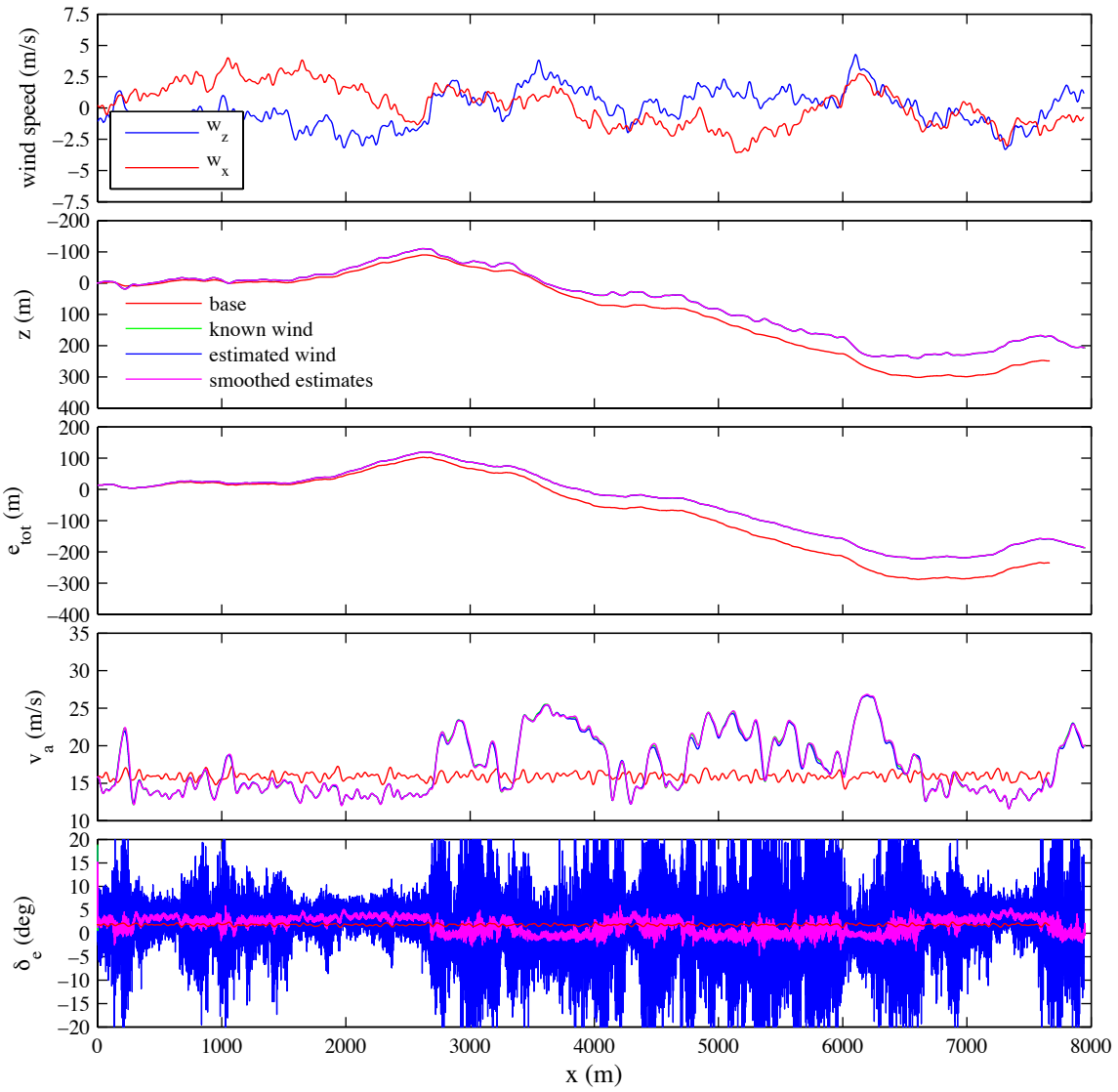

(a) Single run detail

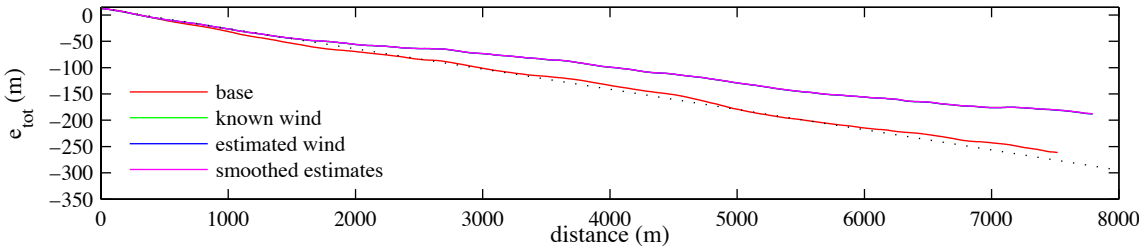

(b) Mean total energy

Figure 10. Performance comparison for flight through Dryden turbulence, medium altitude, light intensity. Baseline (constant airspeed) control shown in red; energy harvesting control with known wind shown in green; energy harvesting control with estimated wind shown in blue; energy harvesting control using smoothed estimates shown in magenta. Subplot (a): upper plot shows true wind field (ix in red, iz in blue); second plot shows flight path; third shows total energy; fourth shows airspeed; fifth (bottom) shows elevator deflection; Subplot (b): mean value of total energy vs. distance over all runs. The dotted black line shows total energy change versus distance for a steady glide in zero wind.

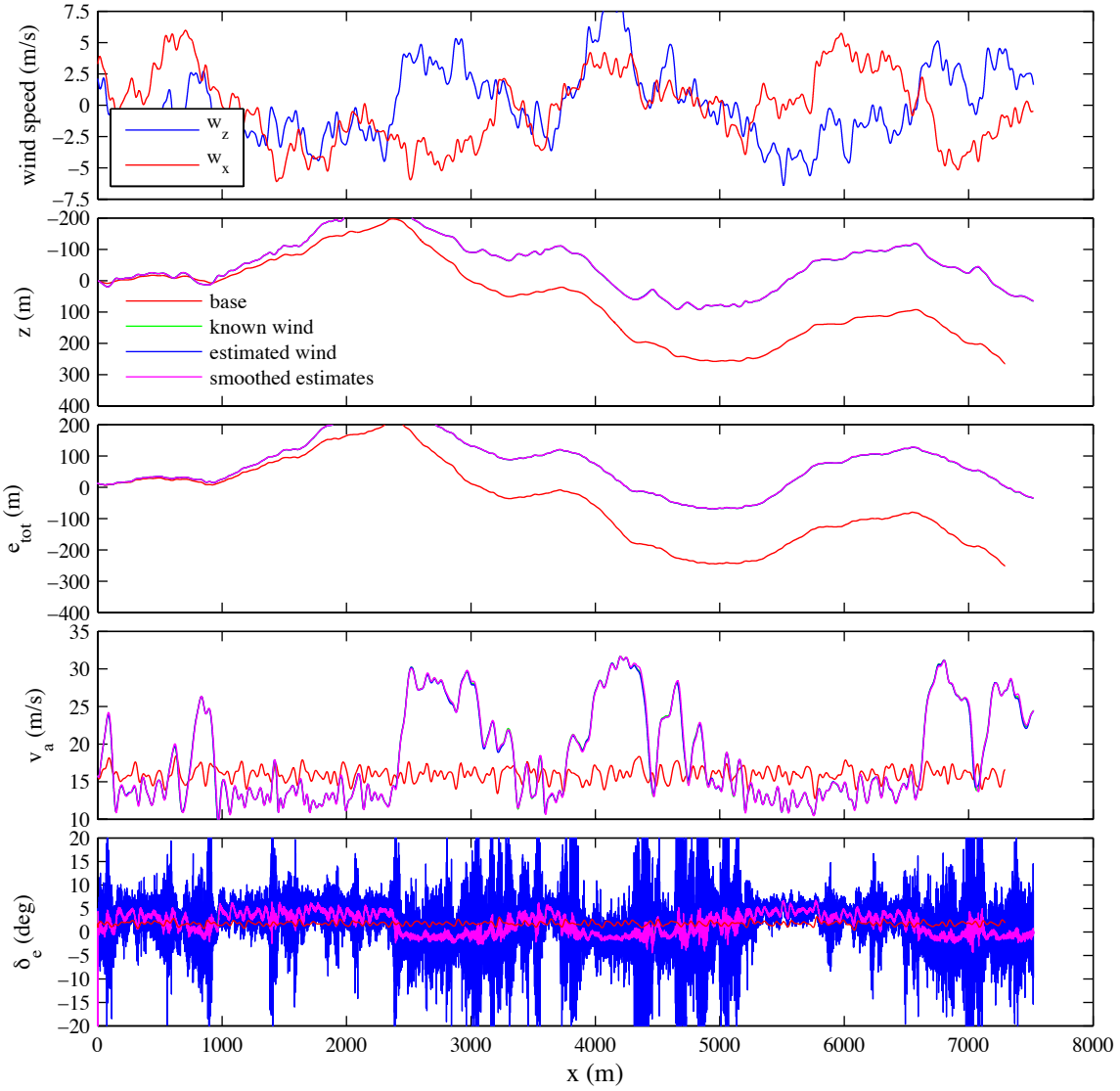

(a) Single run detail

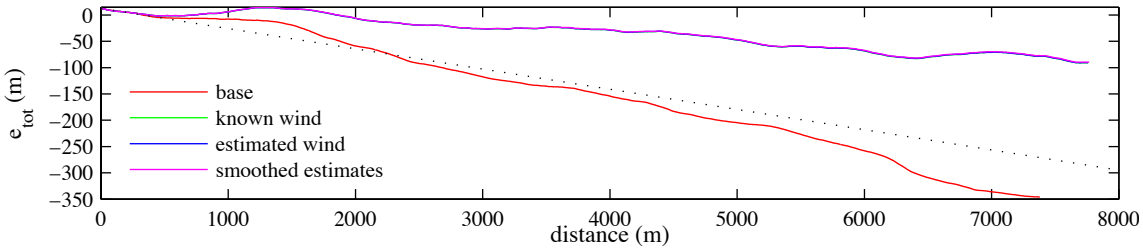

(b) Mean total energy

Figure 11. Performance comparison for flight through Dryden turbulence, medium altitude, moderate intensity. Baseline (constant airspeed) control shown in red; energy harvesting control with known wind shown in green; energy harvesting control with estimated wind shown in blue; energy harvesting control using smoothed estimates shown in magenta. Subplot (a): upper plot shows true wind field (ix in red, iz in blue); second plot shows flight path; third shows total energy; fourth shows airspeed; fifth (bottom) shows elevator deflection; Subplot (b): mean value of total energy vs. distance over all runs. The dotted black line shows total energy change versus distance for a steady glide in zero wind.